

Reynolds Number Effects of a Bird-Feather-Inspired Porous-Medium Airfoil

ZhaoPeng Zhang[1], ZhengYin Ye[1]

[1]School of Aeronautics, Northwestern Polytechnical University, Xi'an, China

Abstract

A bird-feather-inspired anisotropic porous-medium airfoil is proposed in this study. The porous region is designed to be thin near the leading edge and gradually thickened along the streamwise direction, while exhibiting anisotropic permeability to mimic the spatial distribution of bird feathers and their directional resistance to the flow. A Monotone Integrated Large Eddy Simulation (MILES) approach is employed to investigate the Reynolds number effects on the aerodynamic performance of the proposed airfoil over a Reynolds number range representative of small birds' flight conditions ($Re = 4\times10^4$–4×10^5). In addition, a clean airfoil is simulated as a datum condition for comparison. The results indicate that the porous-medium airfoil generally enhances lift, and achieves drag reduction within a certain Reynolds number range. A drag decomposition analysis is conducted to quantify the contributions of lift and drag components at different Reynolds numbers. Further flow-field analyses reveal that the porous-medium structure exhibits significantly different modulation effects on separation vortex structures across different Reynolds number regimes. The bird-feather-inspired anisotropic porous structure exhibits distinct flow control mechanisms across different Reynolds number regimes. These findings provide new insights into the aerodynamic role of bird feather structures in regulating airfoil performance.

Keywords：bird-feather-inspired；porous media；aerodynamic performance；separation vortex structures

1. Introduction

The remarkable aerodynamic characteristics exhibited by birds during flight have provided abundant biomimetic inspiration[1] [2] for fluid mechanics research. In the course of investigating these biological features, it has also been recognized that bird feathers possess structural characteristics analogous to porous media[3] , which may constitute one of the key factors enabling highly efficient flight.

In studies on airfoils incorporating isotropic porous media, Geyer et al.[4] [5] replaced a portion of the trailing-edge structure with isotropic porous materials. Wind-tunnel experiments demonstrated that the presence of the porous structure thickened the

boundary layer, intensified the wake velocity deficit, and significantly enhanced the turbulence intensity above the trailing edge and within the wake region. Seaver et al. [6] experimentally investigated an E591 airfoil with a porous leading-edge section at Reynolds numbers of 60,000 and 150,000. Their results showed that, at higher Reynolds numbers, the porous medium degraded the aerodynamic performance of the airfoil, whereas at lower Reynolds numbers, it increased the stall angle of attack, and a moderate enlargement of the porous region further improved the aerodynamic performance. These findings indicate that the influence of porous media on airfoil aerodynamic characteristics is closely associated with their spatial distribution. Geyer et al.[7] further conducted experiments on an SD7003 airfoil incorporating homogeneous porous media composed of 16 different materials. For manufacturing convenience, the trailing edge of the SD7003 airfoil was thickened. The results showed that the porous airfoil generated lower lift and higher drag compared with the baseline configuration.

Considering that bird feathers exhibit different resistance characteristics to incoming flows from different directions, anisotropic porous airfoils have shown considerable potential in drag reduction and flow-separation suppression. Li et al.[8] experimentally investigated an airfoil equipped with a unidirectionally permeable porous structure distributed near the trailing edge. Their results indicated that the lift and drag characteristics remained nearly unchanged, while the unidirectionally permeable porous structure with relatively low porosity effectively reduced the size of the laminar separation bubble. Zhou et al.[9] performed numerical simulations based on the Shear Stress Transport (SST) model for several NACA airfoils incorporating anisotropic porous media in the leading-edge region under wake disturbances generated by a semicircular cylinder. Although the leading-edge porous medium caused a slight reduction in lift together with drag reduction, the lift generated by the porous airfoil gradually increased with increasing airfoil thickness ratio and eventually exceeded that of the baseline airfoil. In addition, the porous medium significantly suppressed surface pressure fluctuations on the airfoil and weakened near-wall shear effects and vorticity owing to the slip velocity at the porous-medium/fluid interface.

Existing studies on porous-medium airfoils have predominantly focused on placing porous regions near the leading or trailing edges, and Reynolds number effects have been little investigated. Inspired by bird biomimetics, the present study investigates a porous-medium airfoil with a feather-like distribution, with particular emphasis on Reynolds number effects over a range representative of small birds' flight conditions. The porous region is introduced near the leading edge with a streamwise-varying thickness, and anisotropic permeability is prescribed to represent the directional resistance of bird feathers to the flow. Using the Monotone Integrated Large Eddy Simulation[10] (MILES), the Reynolds number effects on lift and drag characteristics as well as separated vortex structures are systematically investigated over a Reynolds number range of 4×10^4 to 4×10^5 representative of small birds' flight conditions. Particular emphasis is placed on identifying the differences in boundary-layer development and separation-vortex modulation mechanisms across Reynolds number ranges. By comparison with a clean airfoil, the aerodynamic impact and potential

advantages of the bird-feather-inspired anisotropic porous structure in low-Reynolds-number flight are clarified.

2. Numerical Methods and Model Formulation

2.1 Governing equation

The governing equations in the fluid domain are numerically solved by MILES. MILES uses the intrinsic dissipation involved in numerical scheme as the implicit small subgrid scale (SGS) model. Due to the simplicity and practicality, MILES has been widely applied in various problems[11] [12].

The porous-medium region is modeled by the Brinkman–Forchheimer equation [13], the governing equations for flow in the porous medium are given by:

$$\begin{cases} \dfrac{\partial \rho}{\partial t} + \nabla \cdot (\rho \boldsymbol{u}) = 0 \\ \dfrac{\partial (\rho \boldsymbol{u})}{\partial t} + \nabla \cdot \left(\dfrac{\rho \boldsymbol{u}\boldsymbol{u}}{\sigma} \right) = -\nabla(\sigma p) + \nabla \cdot \left(\rho \nu \left(\nabla \boldsymbol{u} + \boldsymbol{u} \nabla \right) \right) + \boldsymbol{F} \end{cases} \tag{1}$$

$\boldsymbol{F}$ denotes the body force exerted on the fluid within the porous-medium region, and its expression is given by:

$$\boldsymbol{F} = -\sigma \nu \boldsymbol{K}^{-1} \boldsymbol{u} - \sigma \cdot \frac{C_F}{\sqrt{\boldsymbol{K}}} |\boldsymbol{u}| \boldsymbol{u} \tag{2}$$

Here, $\boldsymbol{K}$ represents the permeability, characterizing the ease with which fluid can flow through the porous medium. In this simulation, a non-dimensional permeability $\boldsymbol{Da}$, $\boldsymbol{Da} = \boldsymbol{K}/L_{ref}^2$ is used. Considering the use of anisotropic porous materials, $\boldsymbol{K}$ is treated as a second-order tensor: when $i \neq j$, $K_{ij}=0$; when $i = j$, $K_{11}=K_x$, $K_{22}=K_z$. C_F also includes an inertial resistance term, and the inertia coefficient is given by the empirical formula proposed by Ergun[14]:

$$C_F = \frac{1.75}{\sqrt{150\sigma^3}} \tag{3}$$

The numerical simulations in the present study were performed using the in-house CFD solver Helios, developed by the authors' research group based on the Fortran programming language. The solver employs the finite-difference method for spatial discretization and utilizes structured grids to achieve high-fidelity numerical simulations. To improve computational efficiency, parallel computing capability is implemented through the Message Passing Interface (MPI). For spatial discretization, a fifth-order dissipative compact scheme is adopted. The inviscid flux terms are discretized using the Roe scheme, whereas the viscous flux terms are treated with a central-difference scheme. Time advancement is carried out using the Gauss–Seidel method. The flow-field variables are nondimensionalized based on the following reference quantities: the freestream density ρ_∞, freestream temperature T_∞, freestream dynamic viscosity μ_∞, freestream speed of sound, and the airfoil chord length c.

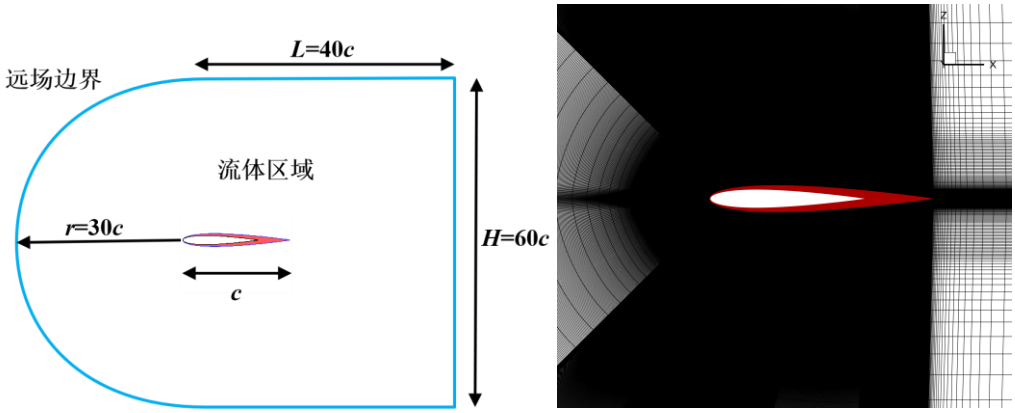
2.2 Model Formulation

The present study considers the NACA0012 airfoil as the research object. A schematic of the computational domain is shown in Figure 1(a). The chord length of the airfoil, c, is taken as the reference length. The far-field semicircular boundary has a radius of r = 30c. The rectangular length L is 40c and height H is 60c.

Considering that the distribution of feathers on bird wings in nature is thin near the leading edge and gradually thickens along the chord, and following construction approaches from previous studies, the NACA0012 airfoil is first scaled to 70% of its original size. The scaled airfoil's leading edge is positioned such that its distance from the original airfoil's leading edge is 0.2%c. In the figure, the black line represents the no-slip wall, the dark blue line represents the interface between the porous medium and the fluid, and the red region denotes the porous-medium area. This configuration of the porous region is designed to mimic the natural feather distribution, being thin at the leading edge and gradually thickening downstream. In addition, a clean airfoil is simulated as a datum condition for comparison.

To model the anisotropic resistance characteristics of bird feathers, an anisotropic porous medium is employed in this study, with a streamwise non-dimensional permeability Da_x = 0.01, a normal non-dimensional permeability Da_z = 0.000001, and a porosity of 0.4.

Based on the flight Reynolds number of small birds, a Reynolds number range of 4×10^4 to 4×10^5 is selected, with an incoming flow angle of attack of 10°. The porous-medium region is discretized using a uniform mesh with a grid height of 3×10^{-5} and a total of 60 layers. The first grid layer at the porous-medium–fluid interface has a height of 5×10^{-5} and a growth rate of 1.05. As shown in Figure 1(b), the red mesh represents the grid within the porous-medium region. The entire computational domain contains 1.33 million grid cells, and this mesh density is sufficient to meet the simulation requirements.



(a) Computational domain (b) Grid domain

Figure. 1 Schematic diagram of computational domain and grid domain

3. Result

Given the complexity of the aerodynamic force generation mechanisms associated with porous airfoils, a decomposition of the aerodynamic forces is required in order to

quantitatively identify their respective contributions.

For a porous airfoil, the total drag can be decomposed into the following components: the skin-friction drag D_f on the solid wall and the porous-medium/fluid interface, the pressure drag D_p on the solid wall and the porous-medium/fluid interface, and the volumetric-force contribution D_{daxi} generated within the porous region. Accordingly, the drag coefficient of the porous airfoil is defined as follows:

$$C_D = \frac{D_p + D_f + D_{daxi}}{\frac{1}{2}\rho V_\infty^2 S_{ref}} \tag{4}$$

where ρ and V_∞ denote the freestream density and velocity, respectively, and S_{ref} represents the reference area of the airfoil.

Similarly, for a porous airfoil, the total lift can be decomposed into the following components: the friction-induced lift L_f on the solid wall and the porous-medium/fluid interface, the pressure-induced lift L_p on the solid wall and the porous-medium/fluid interface, and the volumetric-force contribution L_{daxi} generated within the porous region. Accordingly, the lift coefficient of the porous airfoil is defined as follows:

$$C_L = \frac{L_p + L_f + L_{daxi}}{\frac{1}{2}\rho V_\infty^2 S_{ref}} \tag{5}$$

The pressure coefficient of the porous airfoil is defined as follows:

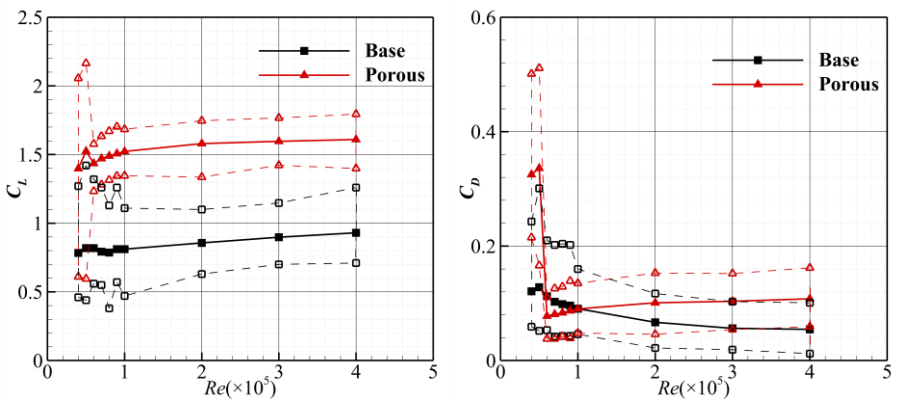
$$C_p = \frac{p - p_\infty}{\frac{1}{2}\rho V_\infty^2} \tag{6}$$

where p denotes pressure and p_∞ denotes freestream pressure.

3.1 Effect of Reynolds Number on the Lift and Drag Characteristics of Porous Airfoils

Figure 2 presents the lift and drag coefficient curves of the baseline airfoil and the porous airfoil at an angle of attack of 10° over the Reynolds-number range Re=4×10^4~4×10^5. In the figure, solid lines denote time-averaged values, while dashed lines represent fluctuation ranges; the black lines correspond to the baseline airfoil, and the red lines correspond to the porous airfoil. As shown in Figure 2(a), within the Reynolds-number range Re=4×10^4~1×10^5, the lift coefficient of the baseline airfoil exhibits large fluctuations without obvious regularity. Over the range Re=2×10^5~4×10^5, the lift coefficient of the baseline airfoil increases gradually, while the fluctuation amplitude decreases. Throughout the computed Reynolds-number range, the time-averaged lift coefficient of the porous airfoil remains consistently higher than that of the baseline airfoil. For Re=6×10^4~4×10^5, the lift coefficient of the porous airfoil continues to increase, and the fluctuation amplitude is smaller than that of the baseline

airfoil. However, within the range Re=4×10^4~5×10^4, anomalous behavior is observed, characterized by a sudden increase in the fluctuation range of the lift coefficient, exceeding that of the baseline airfoil. As observed in Figure 2(b), the drag coefficient of the baseline airfoil decreases continuously over the range Re=5×10^4~4×10^5. For the porous airfoil, both the drag coefficient and its fluctuation amplitude gradually increase within the range Re=6×10^4~4×10^5. Nevertheless, for Re=6×10^4~1×10^5, the drag coefficient and its fluctuation amplitude remain lower than those of the baseline airfoil. In contrast, within the range Re=4×10^4~5×10^4, the porous airfoil exhibits pronounced anomalous behavior, with both the drag coefficient and its fluctuation amplitude increasing sharply. The underlying reasons for the significant differences in lift and drag characteristics at low Reynolds numbers are discussed in the following section.



(a) Lift coefficient curve (b) Drag coefficient curve

Figure. 2 The lift and drag coefficient curves for the baseline airfoil and the porous-medium airfoil

Figure 3 illustrates the lift-to-drag ratio curves of the baseline airfoil and the porous airfoil at an angle of attack of 10° over the Reynolds-number range Re=4×10^4~4×10^5. Within the low-Reynolds-number regime considered in the present study, the baseline airfoil exhibits a very low lift-to-drag ratio, indicating severe aerodynamic performance degradation. As the Reynolds number increases, the lift-to-drag ratio increases monotonically. The porous airfoil alters the sharp deterioration trend of the lift-to-drag ratio observed at low Reynolds numbers, leading instead to a nonlinear variation behavior. In the relatively lower Reynolds-number range Re=4×10^4~5×10^4, the lift-to-drag ratio of the porous airfoil is lower than that of the baseline airfoil. Subsequently, at Re=6×10^4, the lift-to-drag ratio of the porous airfoil increases abruptly, followed by a continuous decrease with further increasing Reynolds number. Moreover, within the range Re=6×10^4~2×10^5, the lift-to-drag ratio of the porous airfoil remains significantly higher than that of the baseline airfoil.

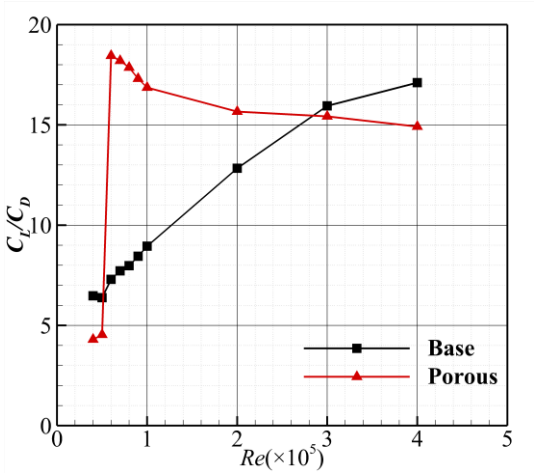
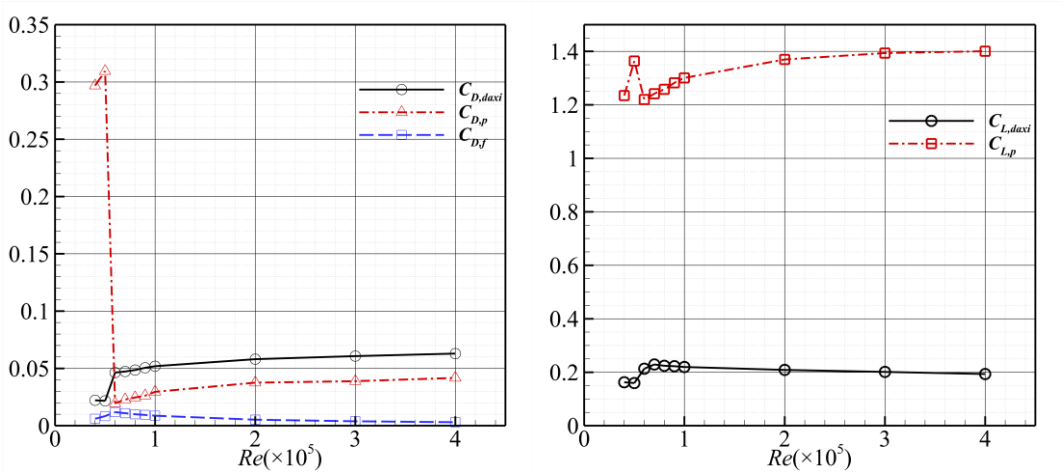


Figure. 3 Reynolds number variation curves of lift to drag ratio for base airfoil and porous media airfoil

To investigate the anomalous lift and drag characteristics observed at low Reynolds numbers, the total lift and drag of the porous airfoil were decomposed, based on the aerodynamic force generation mechanisms, into pressure-induced components, friction-induced components, and porous-medium volumetric-force components, so as to identify the underlying source of the anomaly. The distributions of the various aerodynamic-force contributions under different conditions are presented in Fig. 4. As shown in Fig. 4(a), the pressure contribution dominates the total lift, accounting for more than 80%, whereas the porous-medium volumetric-force contribution exceeds 10%. In contrast, the friction contribution is negligibly small and is therefore omitted from the figure. Within the Reynolds-number range exhibiting anomalous behavior, Re=4×10^4~5×10^4, the relative contribution of the pressure component further increases to nearly 90%, while the contribution of the porous-medium volumetric force decreases to approximately 10%. Although the variation in the lift-contribution proportions is not particularly pronounced, the relative contributions to drag exhibit substantial changes. The results in Fig. 4(b) indicate that, for Re=6×10^4~4×10^5, the friction drag constitutes the smallest portion of the total drag and decreases further with increasing Reynolds number. The porous-medium volumetric-force contribution remains dominant, maintaining a proportion of approximately 60%, whereas the pressure-drag contribution increases with Reynolds number and reaches a maximum value of 39%. However, within the anomalous Reynolds-number range of Re=4×10^4~5×10^4, the pressure drag becomes the dominant contribution, accounting for more than 90% of the total drag. Meanwhile, the contribution of the porous-medium volumetric force decreases sharply to approximately 7%, and the friction-drag contribution remains the smallest, at roughly 3%. These results demonstrate that, in the low-Reynolds-number regime, the anomalous aerodynamic behavior of the porous airfoil is primarily attributed to the differences in the lift and drag contributions induced by pressure forces



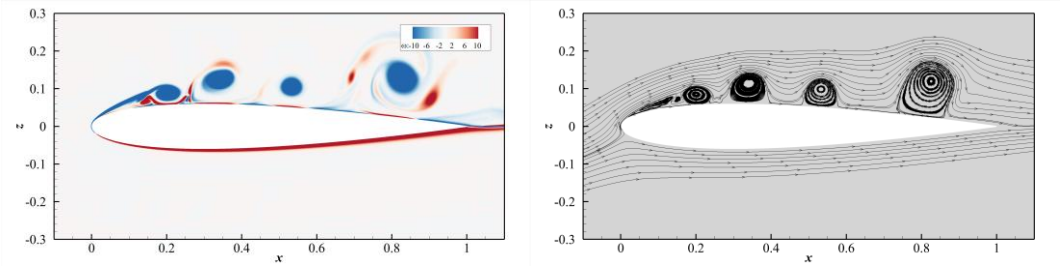
(a) The distributions of the drag (b) The distributions of the lift

Figure. 4 The distributions of the various aerodynamic-force

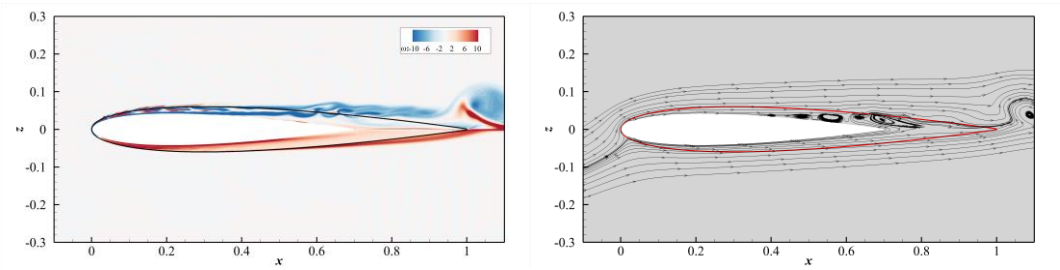
3.2 Effect of Reynolds Number on the Vortex Structure Characteristics of Porous Airfoils

Since the pressure contribution is intrinsically associated with the evolution of vortex structures around the airfoil surface, a further analysis of the flow-field vortex dynamics is conducted in the following section to clarify the underlying mechanism responsible for the anomalous aerodynamic behavior. Figure 5 and Figure 6 presents the instantaneous vorticity contours and streamlines around the airfoil surface at two representative Reynolds numbers, Re=4×10^4 and Re=6×10^4. As shown in Fig. 5, under the condition of Re=4×10^4, the porous airfoil fails to effectively suppress the generation and development of separation vortices. The separation vortex sheds from the leading edge of the airfoil and develops into a large-scale separation region along the streamwise direction. In addition, the reverse seepage flow within the porous region further enhances the local adverse pressure gradient, intensifies momentum exchange, and strengthens the separation vortex. Consequently, at this low Reynolds number, the proportion of pressure drag increases significantly, resulting in a sharp rise in the total drag. The results shown in Fig. 6 indicate that laminar flow separation persists on the surface of the baseline airfoil. However, with increasing Reynolds number, the laminar boundary layer gradually transitions to turbulence. Owing to the stronger resistance of turbulent boundary layers to flow separation, the flow remains more attached to the airfoil surface, and the generated separation vortices subsequently reattach. Meanwhile, the boundary-layer thickness decreases with increasing Reynolds number, leading to larger near-wall velocity gradients and intensified shear motion within the boundary layer. As a result, the number of small-scale vortex structures inside the separation region increases markedly. At Re=6×10^4, the separation vortices formed on the surface of the porous airfoil partially penetrate into the porous region, where they are subjected to the resistance effect of the porous medium. Consequently, the vortices are unable to maintain coherent vortex structures or detach from the wall surface. The strength of the separation vortices is substantially attenuated, thereby preventing the formation of a

large-scale downstream separation region, and only weak vortex shedding is observed near the trailing-edge region of the airfoil. This mechanism explains the increase in the lift-to-drag ratio of the porous airfoil within the Reynolds-number range of Re=6×10^4~2×10^5. The initial separation vortices generated near the leading edge penetrate into the porous region and are suppressed by the resistive effect of the porous medium, preventing vortex shedding from developing along the airfoil surface. This process effectively inhibits the growth and detachment of separation vortices, thereby significantly reducing the pressure drag associated with the separation region and improving the aerodynamic efficiency of the airfoil.

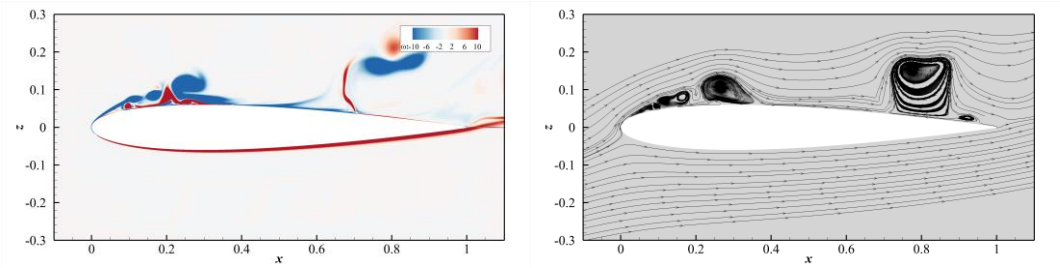


(a) Vorticity contour for base airfoil (b) streamlines contour for base airfoil

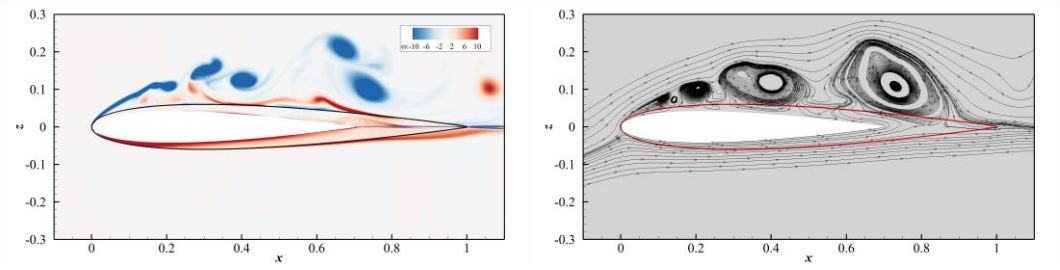


(c) Vorticity contour for porous airfoil (d) streamlines contour for porous airfoil

Figure. 5 Instantaneous vorticity contours and streamlines contours at Re=4×10^4



(a) Vorticity contour for base airfoil (b) streamlines contour for base airfoil



(c) Vorticity contour for porous airfoil (d) streamlines contour for porous airfoil

Figure. 6 Instantaneous vorticity contours and streamlines contours at Re=6×10^4

4. Conclusions

In this paper, the aerodynamic characteristics and vortex structures are investigated. The effect of Reynold numbers on the aerodynamic behaviors is investigated in detail. The main conclusions are as follows.

1. In the relatively lower Reynolds-number range of Re=4×10^4~5×10^4, the separation vortices formed on the surface of the porous airfoil do not penetrate into the porous region. Instead, they are influenced by the reverse seepage flow generated within the porous medium, which enhances the local adverse pressure gradient and further intensifies the separation vortices. As a consequence, the drag acting on the airfoil increases, accompanied by stronger aerodynamic-force fluctuations.

2. Within the Reynolds-number range of Re=6×10^4~4×10^5, the separation vortices formed on the surface of the porous airfoil partially penetrate into the porous region and are suppressed by the resistance effect of the porous medium. As a result, the growth and shedding of the separation vortices are inhibited, preventing the formation of a large-scale downstream separation region. In the absence of vortex shedding, the flow remains attached to the airfoil surface, leading to a substantial reduction in pressure drag and a decrease in aerodynamic-force fluctuations.

The results indicate that the bird-feather-inspired porous airfoil exhibits strong sensitivity to the Reynolds number. Within the Reynolds-number range relevant to bird flight, the porous medium associated with the feather-like structure effectively suppresses the formation and downstream shedding of leading-edge separation vortices under low-Reynolds-number conditions, thereby significantly enhancing the lift and lift-to-drag ratio while simultaneously reducing the fluctuations of aerodynamic forces. However, within the relatively lower Reynolds-number range of Re=4×10^4~5×10^4, the porous medium instead promotes leading-edge flow separation, resulting in an increase in airfoil drag.

Archiving

The ICAS 2026 proceedings will receive an ISSN number and all papers will get individual DOIs.

Contact Author Email Address

zzp99@mail.nwpu.edu.cn

Copyright Statement

The authors confirm that they, and/or their company or organization, hold copyright on all of the original material included in this paper. The authors also confirm that they have obtained permission, from the copyright holder of any third party material included in this paper, to publish it as part of their paper. The authors confirm that they give permission, or have obtained permission from the copyright holder of this paper, for the publication and distribution of this paper as part of the ICAS proceedings or as individual off-prints from the proceedings.

References

[1] Aboelezz A, Herkenhoff B, Hassanalian M. Effects of Avian Wings Color Patterns on Their Flight Performance: Experimental and Computational Studies[J]. *Journal of Bionic Engineering*, 2023, 20(2): 683-711.

[2] Pellerito V, Hassanalian M, Sedaghat A, et al. Performance analysis of a bioinspired albatross airfoil with heated top wing surface: experimental study[C]//AIAA Propulsion and Energy 2019 Forum. 2019: 4319.

[3] Quan P, Zhong S, Liu Q, et al. Attenuation of flow separation using herringbone riblets at M∞= 5[J]. *AIAA Journal*, 2019, 57(1): 142-152.

[4] Geyer T, Sarradj E. Trailing edge noise of partially porous airfoils[C]//20th AIAA/CEAS aeroacoustics conference. 2014: 3039.

[5] Geyer T, Sarradj E, Fritzsche C. Porous airfoils: noise reduction and boundary layer effects[J]. *International journal of aeroacoustics*, 2010, 9(6): 787-820.

[6] Seaver E, Laporte H. Experimental analysis of the effects of porous media on airfoil performance[C]//AIAA SCITECH 2024 Forum. 2024: 2328.

[7] Geyer T, Sarradj E, Fritzsche C. Measurement of the noise generation at the trailing edge of porous airfoils[J]. *Experiments in fluids*, 2010, 48(2): 291-308.

[8] Li J, Nagata K, Watanabe T. Large-eddy simulation of low-Reynolds-number flow around partially porous airfoils[J]. *Journal of Aircraft*, 2023, 60(6): 1998-2009.

[9] Zhou Z, Wang Y. Numerical simulation study of the effect of porous media passive flow control on the propulsion performance of airfoils in kármán vortex streets[J]. *Ocean Engineering*, 2024, 311: 118720.

[10] Boris J P, Grinstein F F, Oran E S, et al. New insights into large eddy simulation[J]. *Fluid dynamics research*, 1992, 10(4-6): 199.

[11] Hahn M, Drikakis D. Large eddy simulation of compressible turbulence using high-resolution methods[J]. *International journal for numerical methods in fluids*, 2005, 47(8-9): 971-977.

[12] Fureby C, Grinstein F F. Monotonically integrated large eddy simulation of free shear flows[J]. *AIAA journal*, 1999, 37(5): 544-556.

[13] Nithiarasu P, Seetharamu K N, Sundararajan T. Natural convective heat transfer in a fluid saturated variable porosity medium[J]. *International Journal of Heat and Mass Transfer*, 1997, 40(16): 3955-3967.

[14] Ergun S. Fluid flow through packed columns[J]. *Chemical engineering progress*, 1952, 48(2): 89.